Irrigation-driven groundwater depletion in the Ganges-Brahmaputra basin decreases the streamflow in the Bay of Bengal

Fadji Z. Maina[1,2*], Augusto Getirana[1,3], Sujay V. Kumar[1], Manabendra Saharia[4], Nishan Kumar Biswas[1,2], Sasha McLarty[5], Ravi Appana[5]

[1] NASA Goddard Space Flight Center, Hydrological Sciences Laboratory, Greenbelt, Maryland, USA
[2] University of Maryland, Baltimore County, Goddard Earth Sciences Technology and Research Studies and Investigations, Baltimore, Maryland, USA
[3] Science Applications International Corporation, Greenbelt, Maryland, USA
[4] Department of Civil Engineering, Indian Institute of Technology, Delhi, India
[5] Washington State University, Pullman, Washington, United States

*Corresponding Author: fadjizaouna.maina@nasa.gov

Abstract

Ganges and Brahmaputra, two of Asia's most prominent rivers, have a crucial role in Southeast Asia's geopolitics and economy and are home to one of the world's biggest marine ecosystems. Irrigation-driven groundwater depletion and climate change affect the Ganges-Brahmaputra's hydrology, threatening the stability of the Bay of Bengal. Here, we quantify, using results from a land reanalysis, the impacts of a changing climate and intensive irrigation on the surface water flowing into the Bay of Bengal. The effects of such activities mostly occurring in the Ganges basin, either intensified or lessened depending on the area by the climatic conditions, decrease freshwater flow into the bay by up to 1200 m^3/s/year. While the increase in precipitation in the Ganges basin reduces the effects of groundwater depletion on the streamflow, the decrease in precipitation and the snowmelt decline in the Brahmaputra basin exacerbate streamflow reduction due to groundwater depletion at the delta.

1. Introduction

Climate change and agricultural activities have serious consequences that are yet to be quantified on Asia's most prominent river basins. Located in a densely populated area, the basins of the Ganges and Brahmaputra Rivers cover six countries: India, Myanmar, Bhutan, Nepal, China, and Bangladesh (Figure 1). These rain- and snow- fed transboundary rivers are critical for the lives of more than a billion people[1–3] and have allowed civilization to develop and thrive along their tributaries for centuries. The Ganges River, with a draining area of approximately 1,086,000 km^2, takes its source in the glaciated area of Gomukh in the Himalaya Mountains and merges with the Brahmaputra River, with a draining area of around 500,000 km^2, which also originates from the Himalayas in the glaciated zone of Lake Mana Sarovar, before emptying out into the Bay of Bengal. The Bay of Bengal plays a vital role in global geopolitics and economy due to its strategic geographical location in Southeast Asia. The Bay of Bengal also hosts one of the biggest marine ecosystems and the Sundarbans, which are the largest mangrove forests on Earth[4] and have vast deposits of hydrocarbon resources and mineral wealth. Therefore, upstream changes in streamflow caused by groundwater depletion and climate change can impact the ecosystem, economy, and geopolitics of the bay as well as its inhabitants[5].

Like the greater region, the so called High Mountain Asia, the Ganges-Brahmaputra basin experiences warming at a rate that is double the global average (0.32°C per decade compared with the global average of 0.16°C per decade), making it one of Earth’s most vulnerable basins[1]. Because the basin is subject to glacier and snow melt, extreme monsoons, and sea level rise, climate change will likely intensify the hydrologic cycle. Warming in the region has increased precipitation and decreased snowpack and glaciers[2,6–8], which significantly impact groundwater and streamflow. Moreover, changes in precipitation phase (i.e., more precipitation is falling in the form of rain than snow) shift the dynamics and the seasonality of the land surface processes with consequences on water management and hazards[7,9,10]. In addition to these natural changes, the Ganges-Brahmaputra basin has the highest rate of groundwater use on Earth[11–13] with India withdrawing about 230 billion m^3 of groundwater annually for irrigation[14]. As a result, significant groundwater depletion has been documented in the region[15–17] with dramatic consequences on streamflow[5,18,19], which has been decreasing in the Ganges River despite an increasing trend in precipitation[19]. The unprecedented changing climate, along with human footprints has caused the vegetation to rapidly change[20,21]. The region experiences one of the highest greening rates on Earth, altering the water and energy balances[20,22,23]. This moisture-induced greening, triggered by irrigation, decreases in snow, and increases in precipitation affect the surface albedo and hence the climate system and the water resources[21,24].

A holistic and cumulative assessment of the impact of all these factors on the water availability over the Bay of Bengal is currently lacking. Therefore, we focus on disentangling the impacts of groundwater depletion and climate change on the Bay of Bengal's freshwater flow, as it has important implications for the sustainable management of water resources[11,25] in this region. Changes in streamflow can intensify water scarcity and food insecurity and worsen the already devasting floods affecting the economy and the lives of the inhabitants of this basin. Moreover, a declining streamflow in the Bay of Bengal may accelerate the impacts of sea level rise and seawater intrusion, with consequences on water quality, environment, and human migrations. In this study, we provide a comprehensive examination of the impacts of the interactions between groundwater depletion and changes in climate (i.e., increases and decreases in precipitation and decreases in snowmelt due to warming) over the entire Ganges-Brahmaputra basin. Comparatively, prior studies have only focused on the influence of groundwater depletion on streamflow reduction over the Ganges basin alone[19]. Integrating the entire basin is necessary to better understand and quantify the contribution of the drivers of the changes in streamflow in the Bay of Bengal. To represent the impacts of irrigation-driven groundwater depletion, we develop a land surface model reanalysis from 2003 to 2020 by assimilating remote-sensing based observations of irrigation, Terrestrial Water Storage (TWS), leaf area index (LAI), and snow water equivalent (SWE) into the land surface model Noah-Multi-Parameterization (Noah-MP[26]).

2. Results and Discussion

The land surface model reanalysis has been validated by comparing the trends in simulated key hydrologic variables such as streamflow (Supplementary Figures 4 and 5), runoff and groundwater storage (Supplementary Figure 6), and evapotranspiration (Supplementary Figure 7) to the trends derived from ground and remotely sensed measurements. We also evaluate the probability of snow detection of our model (Supplementary Figure 8). We mainly focus on the evaluation of the simulated trends since the main purpose of this study is to shed light on the causes of the observed trends in streamflow in the region. To quantify the effects of groundwater pumping for irrigation, we compare the simulation with the effects of irrigation (i.e., land surface model reanalysis) to a simulation performed by only accounting for the impacts of a changing climate (i.e., changes in precipitation and decreases in snow). Our results reveal the severe effects of irrigation-driven groundwater depletion on the streamflow in the Bay of Bengal. Irrigation-driven groundwater depletion occurring upstream in the Ganges-Brahmaputra basin decreases the streamflow in the Bay of Bengal by up to 1200 m^3/s/year despite the increase in precipitation in the Ganges basin. While the increase in precipitation in the Ganges basin (up to ~315 mm/year in the western Ganges) reduces the effects of the declining groundwater storage on the streamflow upstream, the reduction in precipitation at a rate of ~22 mm/year and the declining snowmelt in the Brahmaputra basin exacerbate the impacts of groundwater depletion on its streamflow. Therefore, although groundwater depletion in the Ganges basin is the highest, the Brahmaputra basin has the highest decrease in streamflow increasing its vulnerability to groundwater depletion and sea level rise.

2.1.Synergistic impacts of groundwater depletion and climate change on Bay of Bengal's water availability

The streamflow has a decreasing trend of more than 200 m^3/s/year from 2003 to 2020 in most areas of the Ganges-Brahmaputra basin, but the Bay of Bengal has the highest loss in streamflow (1200 m^3/s/year, Figure 2a). However, the Chambal and Betwa basins, located on the southwestern edge and tributaries of the Ganges River, are characterized by a rise in streamflow of about 60 m^3/s/year. Streamflow reduction is more pronounced in the Brahmaputra, reaching

1000 m^3/s/year than in the Ganges, especially upstream where these decreases are of the order of 100 m^3/s/year. Such a decline in streamflow is not detected when only considering the changes in climate (i.e., an increase in precipitation and a decrease in SWE due to warming) in modeling. In such simulations, where only climate impacts are considered and without the effects of irrigation, streamflow has an annual increase of around 100 m^3/s/year in the Ganges basin whereas streamflow in the Brahmaputra basin has no significant trends (Figure 2g and Supplementary Figures 1, 2, and 3). Therefore, these decreases in streamflow are likely not caused by climate dynamics, rather by the anthropogenic activities. Similar trends are depicted in Figure 3, illustrating the annual mean, minimum, and maximum simulated streamflow in the Ganges and the Brahmaputra rivers at the Bay of Bengal. Without accounting for irrigation, the streamflow of the Ganges basin has an increasing trend up to 552 m^3/s/year during peak flow, whereas with the impacts of irrigation, the streamflow is decreasing by up to 803 m^3/s/year. In the Brahmaputra basin, irrigation practices change the trends in the streamflow from a statistically no significant trend to a decreasing trend up to 1024 m^3/s/year.

In the Ganges-Brahmaputra basin, the precipitation has a bidirectional trend, with an overall increasing trend in the Ganges basin of 315 mm/year locally and a decreasing trend in the Brahmaputra basin reaching ~22 mm/year locally (Figure 2b). Though very localized, some areas of the Brahmaputra basin (i.e., over Bhutan) are characterized by a noteworthy increasing trend in precipitation greater than 20 mm/year. Despite the significant increase in precipitation in the Ganges basin, our results reveal statistically significant decreases in streamflow. The Ganges basin is subject to intense agricultural activities, which cause a loss in TWS locally of up to 50 mm/year (Figure 2c). Only the Chambal and Betwa basins show rising trends in TWS greater than 10 mm/year because their catchments are not subject to intense pumping and experience an increase in precipitation. Groundwater depletion led the subsurface flow to decline by 0.21 mm/d/year in the Ganges basin (Figure 2e). Nonetheless, these trends remain twice lower than the decreases in subsurface flow in the Brahmaputra basin (>0.27 mm/d/year), where the decreases in TWS (20 mm/year) are inferior to those observed in the Ganges basin. Although both rainfall and snowmelt decline over the Brahmaputra basin (Figures 2b and f), there are no statistically significant trends in streamflow in most areas of the basin when accounting only for the changes in climate (Supplementary Figure 1). This is likely because of the influence of the localized increase in precipitation occurring in the other regions of the basin (i.e., high elevation zones of Bhutan and Bangladesh) on the streamflow. The streamflow reduction as well as the decreases in subsurface flow in the Brahmaputra basin, which is subject to smaller declines in TWS, are higher than those over the Ganges basin (characterized by high declines in TWS). This is because the effects of groundwater depletion are exacerbated by the decrease in precipitation in the Brahmaputra basin though such climatic factors alone are not sufficient to trigger statistically significant decreases in streamflow (as shown in the simulation with only the impacts of a changing climate, Figure 2g and Supplementary Figures 1, 2, and 3). In the Ganges basin, the impacts of groundwater depletion on streamflow remain relatively low because (1) the high increase in precipitation reduces the effects of the decrease in groundwater storage and TWS, even though the basin receives lower total precipitation than the Brahmaputra basin; and (2) the Chambal and Betwa Rivers flowing into the Ganges River contribute to further dampening streamflow due to their positive trends.

2.2. Synergic effects of irrigation and climatic conditions decrease the dry-season streamflow in the Ganges basin and the monsoon streamflow in the Brahmaputra basin

In the Ganges basin, precipitation significantly increases during both the dry season (14.6 mm/year from December to February, 21.9 mm/year from March to May) and the monsoon (>100 mm/year from June to August, the maximum rise in annual precipitation, Figure 4). Though TWS shows a decrease throughout the year, the highest loss, up to 55 mm/year, occurs during the monsoon. The maximum decrease in subsurface flow is in the dry season from December to February (0.2 mm/d/year) and from September to November (0.16 mm/d/year) when the increasing trends in precipitation are small and the total precipitation is low compared to the monsoon precipitation. The increase in precipitation (>70 mm/year) in the Chambal and Betwa basins mostly occurs during the monsoon. As a result, monsoonal TWS and subsurface flow have remarkable increases of about 5 mm/year and 0.14 mm/d/year, respectively. Although the highest decline in TWS occurs during the monsoon, the decreases in streamflow are more preponderant in the post-monsoon season from September to November because the post-monsoon precipitation is not sufficient to diminish the impacts of groundwater pumping for irrigation.

A different behavior is observed in the Brahmaputra basin, which experiences decreases in monsoon precipitation by up to 182 mm/year (Figure 4a, JJA). The decreasing trends in precipitation are very low or statistically insignificant during the dry season. As a result, the annual trend in precipitation is mostly driven by the trends in monsoon rainfall. However, we note that, locally, there are significant increases in monsoon precipitation within the basin, which explain the occurrences of floods. Even though the decrease in TWS is two times lower than that over the Ganges (Figure 2c), the decreases in subsurface flow are four times higher in the Brahmaputra basin than in the Ganges basin (Figure 2e). These reductions in subsurface flow are preponderant (>0.87 mm/d/year) during both the monsoon (from June to August) and the dry season (from September to November), yet during the monsoon, the highest decline in the subsurface flow was observed because most of the decrease in rainfall is during that period. As for the subsurface flow, the largest reduction in streamflow is during the monsoon, reaching up to 1800 m^3/s/year downstream even though the majority of the rainfall in the Brahmaputra basin falls during that season. In addition to the monsoon rainfall, snowmelt reaches its maximum in summer[74] and increases the streamflow. The combination of the decline in snowmelt in the summer (Figure 2f) and the decreases in monsoon rainfall exacerbates the effects of groundwater depletion on the streamflow in the Brahmaputra basin. Such climatic changes make the Brahmaputra basin very vulnerable to groundwater depletion.

Both Ganges and Brahmaputra Rivers are characterized by decreasing trends in streamflow, though with different magnitudes flow into the Bay of Bengal. Therefore, the changes in streamflow in the bay are important (>1800 m^3/s/year) notably from June to August, i.e., during the monsoon due to the compounding effects of groundwater withdrawals, decrease in precipitation, and snowmelt decline.

2.3. Long-term impacts of irrigation-driven groundwater depletion on the streamflow versus the impacts of climate change

With the onset of climate change, projections are important and provide guidelines for future strategies. However, most of the future projections of the changes in hydrologic dynamics and water resources in the Ganges-Brahmaputra basin solely rely on climatic conditions [27–30]. As such, these studies predict an increase in streamflow due to an increase in precipitation[27–30]. Nevertheless, irrigation-driven groundwater depletion could actually change the direction of the trends in water availability. Because of the significant impacts of groundwater withdrawals on streamflow, it is essential to account for them in future projections.

Due its climatic conditions, the Brahmaputra basin is highly vulnerable to groundwater depletion; unfortunately, decreases in precipitation and snowmelt could further increase the rates of pumping, with serious consequences on the streamflow, notably in the Bay of Bengal, and therefore on water availability. Such behaviors intensify drought conditions, make the drought recovery longer[31], worsen water scarcity, and enhance the vulnerability of the basin. Because both basins empty into the Bay of Bengal, the decreases in streamflow in the bay are noteworthy. A decline in streamflow may intensify sea level rise and seawater intrusion, with consequences on the environment and water quality. Future studies could analyze the impacts of a decrease in precipitation on pumping rates and applied irrigated water and their subsequent effects on streamflow reduction in the Bay of Bengal. For example, projections have shown that the consumption of nonrenewable water resources will increase by around ~40% by the end of the century[32], as such, future studies could use this water use projection in conjunction with climatic projection to better estimate changes in streamflow and quantify the impacts of such rise in freshwater use on sea level rise. Because these rivers are recharged by glaciers, the increase in temperature causing glacier melt could increase the streamflow. Nonetheless, our results show that the streamflow keeps decreasing, and such trends are consistent with observations. Although we did not account for glacier melt in our model, the assimilation of GRACE TWS implicitly accounts for the global changes in TWS. In addition, previous studies have shown that the contribution of glacier melt to the streamflow is low i.e., less than 10%[19]. Irrigation also impacts the land surface processes by changing the precipitation patterns, nonetheless, we did not study these impacts in our study as changes in precipitation measured by remotely sensed platforms are defined as model inputs, thereby, any changes in precipitation resulting from irrigation has been accounted for.

Methods

The quantification of the changes in streamflow in the Ganges-Brahmaputra basin is challenging due to the complex dynamics of the basin. First, an accurate representation of the atmospheric dynamics of the region is difficult to undertake due to the harshness of the environment, which is not easily accessible due to its complex orographic patterns and its high elevation[33–35]. As a result, climate dynamics are poorly constrained and forcing products derived from satellite remote sensing and/or models fail to provide consistent estimates[36]. Second, the spatiotemporal variations of human footprints are difficult to estimate due to a lack of data. For example, accurate estimates of the spatiotemporal variations of irrigation and pumping are not available. Third, the lack and/or the limited amount of available ground measurements of hydrologic variables make the model evaluation and comparison difficult to perform, making some uncertainties irreducible. In this study, we rely on multiple observation-based datasets to reduce these uncertainties. First, we develop an ensemble consensus precipitation estimates using the Integrated Multi-satellitE Retrievals for Global Precipitation Measurement IMERG[37], the Climate Hazards group Infrared Precipitation with Stations CHIRPS[38], and the ECMWF Reanalysis ERA5[39], which were blended by using the probability matched method[40]. We selected these products after comparing the averages and trends in seven widely used gridded precipitation products in the region[36]. Second, we assimilate five different variables to account for the anthropogenic activities in the region and better constrain our model. We use the Noah-Multi-Parameterization (Noah-MP[26] version 4.0.1) land surface model to simulate the land surface processes in the Ganges-Brahmaputra basin and to assimilate the selected variables from 2003 to 2020. We select this time frame based on the availability of the assimilated datasets. The Noah-

MP model is run at a spatial resolution of 5 km and a temporal resolution of 15 minutes. The simulations were performed within the NASA Land Information System (LIS[41]).

1. Model set-up

Noah-MP represents the next generation of the Noah land surface model development and incorporates extensive upgrades, including dynamic vegetation phenology, a carbon budget and carbon-based photosynthesis, an explicit vegetation canopy layer, and the addition of an unconfined groundwater aquifer[26]. Moreover, Noah-MP allows a representation of irrigation processes and groundwater withdrawals. In Noah-MP, the surface energy balance is computed at both the canopy layer and the ground surface. In the canopy layer, a two-stream radiation transfer approach along with shading effects are used to accurately compute the surface energy and water transfer processes following[42,43]. The model's vegetation dynamics follow Dickinson's et al. approach[44]. The model also combines a Ball-Berry photosynthesis-based stomatal resistance[45]. The soil with a depth of 2 m is divided into four layers, and the water movement is simulated using the Richards equation[46]. An unconfined aquifer is added below the 2 m of the soil column. The temporal variation of the groundwater storage in the unconfined aquifer is equal to the difference between the recharge rate calculated using Darcy's law and the discharge. Groundwater discharge and surface runoff are simulated using the TOPMODEL approach which consists of expressing these terms as exponential functions of the water table depth[26,47,48]. The water table depth is converted from the aquifer water storage by using the specific yield, which is a constant equal to 0.2.

We drive the land surface model Noah-MP simulations with the ensemble precipitation dataset and downscaled ERA5 surface meteorology[49,50] (temperature, shortwave, and longwave radiation, wind speed, relative humidity, and surface pressure). The model uses high-resolution datasets of elevation, slope, and aspect derived from the Multi Error Removed Improved Terrain (MERIT[51]) Digital Elevation Model, the landcover data derived from the Moderate Resolution Imaging Spectroradiometer (MODIS[52]) at a resolution of 500 m, soil types derived from the International Soil Reference and Information Centre[53] at 250 m resolution. The initial conditions for the model simulations are generated by running the model twice from 1990 to 2018 and reinitializing it in 2003.

To simulate the surface water dynamics, including streamflow, we use the Hydrological Modeling and Analysis Platform (HyMAP[54]). HyMAP is a state-of-the-art, globalscale flood model capable of simulating surface water dynamics, including water storage, elevation and discharge in-stream, in rivers and floodplains. In LIS, HyMAP is coupled with numerous land surface models, including Noah-MP. Users can choose different methods to solve the full momentum equation of open channel flow[55]. Here, we adopted the kinematic wave equation. The Courant–Freidrichs–Levy (CFL) condition was used to determine HyMAP's optimal sub timesteps. River geometry were derived from global empirical equations[54]. River network parameters were derived from the Multi-Error-Removed Improved-Terrain (MERIT) Hydro dataset at 3-arcsec spatial resolution[56]. The model simulates horizontal water fluxes over continental surfaces where the runoff and baseflow generated by Noah-MP are routed through a prescribed river network to oceans or inland seas.

2. Assimilations

Data assimilation approaches consist in improving the model estimates by merging measurements of any type including remote sensing observations to the model estimates[57,58]. The latter are updated to reflect the observations to be assimilated by accounting for the model and the observation errors (indicated in Supplementary Table 1). The assimilation is performed at any grid cell and time step whenever the observations are available. We assimilate five variables: (1) applied irrigated water provided by Zhou et al.[59] (2) soil moisture provided by the European Space Agency Climate Change Initiative (ESA CCI[60]), (3) LAI provided by MODIS[61], (4) SWE provided by Kraaijenbrink et al.[62], and (5) TWS provided by the GRACE GSFC mascons[63] during the entire period of our simulation i.e., from 2003 to 2020. The applied irrigated water was directly added to the model as a source of water (which is extracted from the groundwater), and the simultaneous assimilation of LAI, soil moisture, and SWE was based on the one-dimensional ensemble Kalman Filter (EnKF[64]) algorithm, and GRACE TWS was assimilated using the one-dimensional ensemble Kalman smoother (EnKS[65]). EnKF is the optimal sequential data assimilation method for nonlinear dynamics and has been widely used to assimilate remotely sensed variables into the land surface model Noah-MP[66–70].

- **Irrigation**

We assimilate spatiotemporal values of applied irrigated water generated by combining a static irrigation dataset the Global Irrigated Area Map (GIAM), and a time-varying irrigation map for India from Ambika et al.[71], which is generated by combining yearly MODIS - Normalized Difference Vegetation Index (NDVI) data, Indian Remote Sensing Land Use and Land Cover data, and vegetation condition index data. The applied irrigated water dataset has a resolution of 0.05º, like our model. Therefore, we directly added these estimates as a water source in the model using the sprinkler irrigation scheme. Though other irrigation schemes are used in the region, a shift in irrigation practice is not likely to have an impact on the results in terms of groundwater depletion as the latter has been represented by assimilating remotely sensed data. We assumed that the applied irrigated water originates from groundwater as previous studies have demonstrated that irrigated water in HMA mostly originates from groundwater – groundwater accounts for more than

80% of irrigated water – which explains the high decline of groundwater in India[17,31]. However, because of the setting of the model, we deducted all the applied irrigated water from groundwater. Because we assimilated the TWS provided by GRACE to model the depletion of groundwater due to irrigation, the choice of the source of the applied irrigated water is relatively inconsequential in impacting groundwater changes. Future studies can investigate the impacts of the source of the applied irrigated water on the hydrologic system. Following Nie et al.[72], the irrigation scheme implanted in Noah-MP subtracts the groundwater irrigation amount from the model's groundwater storage term, and the water table depth and groundwater storage are updated accordingly. Though irrigation impacts the atmospheric dynamics by changing the precipitation patterns, we did not model these effects because the precipitation is set as a model input in Noah-MP.

- **Soil Moisture**

We assimilated the combined ESA CCI soil moisture v05.2 generated by blending the soil moisture retrievals from active and passive microwave remote sensing instruments. The ESA CCI soil moisture, with a spatial resolution of 0.25°, was downscaled to the resolution of our model using the nearest neighbor approach. For the assimilation of soil moisture, as described by Kumar et al.[66], the observations are rescaled to the model climatology using the cumulative density function (CDF). CDFs are derived separately from both the ESA CCI soil moisture retrievals and the soil moisture simulated by Noah-MP at each grid point during the entire simulation period following Kumar et al.[66,73].

- **Leaf Area Index (LAI)**

Because of the irrigation-induced greening in the Ganges-Brahmaputra basin, the assimilation of LAI is essential to better incorporate these changes in land surface processes. Moreover, the assimilation of LAI has been shown to help improve the simulation of the water budget and the representation of hydrodynamics in irrigated lands[74]. We assimilate the LAI values provided by the MCD15A2H Version 6 of MODIS[61] at a spatial resolution of 500 m and a temporal resolution equal to 8 days following Kumar et al.[74]. The MCD15A2H LAI was upscaled to the model resolution using the average procedure. In this assimilation framework, the updated LAI from assimilation is used to update the leaf biomass by dividing the LAI value with the specific leaf area, which varies with vegetation type, consistent with the Noah-MP physics formulations[75]. However, other vegetation mass prognostic variables in Noah-MP related to the stem, wood, and root mass are not updated as part of the assimilation. The assimilation of LAI is performed using the EnKF algorithm, therefore, we perturbed the different variables to capture the errors.

- **Snow Water Equivalent (SWE)**

We assimilate the SWE reconstruction developed by Kraaijenbrink et al.[62], which employs a temperature index melt model[76] along with ERA5 forcing, and MODIS snow cover[77] to develop multidecadal estimates of SWE. The dataset has a spatial resolution similar to our model and we applied the nearest neighbor approach to project the SWE values to the model grid. More details about the SWE model calibration and evaluation can be found in[62]. The SWE assimilation methodology is described by Kumar et al.[74].

- **Terrestrial Water Storage (TWS)**

Due to high decreases in TWS caused by anthropogenic activities observed in the Ganges-Brahmaputra basin, the assimilation of GRACE TWS is important since these processes cannot be represented in the natural system due to the lack of accurate estimates of anthropogenic activities. The assimilation of GRACE will improve the representation of groundwater depletion and irrigation processes. We assimilate the TWS provided by GRACE GSFC mascon product which has a resolution of 0.5° using the EnKS algorithm as described by Zaitchik et al. and Kumar et al.[65,78]. GRACE GSFC mascon product was downscaled to the resolution of our model by using the bilinear interpolation technique. In this method, GRACE observations are assimilated into the model at the monthly scale, whenever the observation is available. The assimilation of GRACE TWS was performed in two iterations for each month. The EnKS first generates the model predicted TWS observations by averaging simulated TWS. These predictions are then used to calculate the assimilated increments for the month. Next, the second iteration consists of applying these increments. Irrigation is applied during both the first and the second iteration to account for groundwater withdrawal for irrigation in the calculation of TWS.

- **Multivariate Assimilation**

A model ensemble of size 20 was created by perturbing the hourly meteorological forcing inputs (precipitation, downward longwave and shortwave radiation), the modeled (e.g., soil moisture, LAI, SWE, snow depth, and groundwater storages), and the observed variables derived from observations. The selected perturbations are shown in Supplementary Table 1.

In addition to the multivariate assimilation (i.e., simulation of the impacts of irrigation), we also perform a simulation without the impacts of the irrigation by solely accounting for the changes in climate; we, therefore, only assimilate SWE in this simulation. The simulation without the impacts of irrigation will allow investigating the impacts of irrigation (changes in soil moisture, LAI, and TWS) on the system.

3. Model Validation

The model validation consists in evaluating the simulated streamflow, runoff, groundwater storage, ET, and snow cover. We compared the outputs of our model with remotely sensed observations and ground measurements that have not been assimilated in the model from 2003 to 2020. We mainly compared the trends of the different variables because of the main purpose of this study is to understand the causes of the decreasing trends in streamflow. Because of the lack of sufficient data, we did not assimilate streamflow in the region, however, we expect the different assimilations to affect the streamflow. Therefore, we compare the simulated streamflow to observations collected at two gages located in both the Ganges River and the Brahmaputra River. Overall, the comparisons (illustrated in Supplementary Figures 4 and 5) of the trends and the averages of streamflow indicate that the simulations with the impacts of irrigation (i.e., multivariate assimilation) has allowed to significantly improve the modeled hydrodynamics and the obtained results are consistent with the observations. We note that our simulations overestimate the measured baseflow and underestimate the measured peak flow (Supplementary Figure 5). However, because the study is targeting the trends, these biases are not affecting the overall trends as shown by the comparisons of the trends in Supplementary Figure 2. We also compare the simulated trends in runoff and groundwater storage to the trends in runoff data provided by Ghiggi et al.[79] and groundwater storage derived from ground measurements (Supplementary Figure 6). Our multivariate assimilation allows reproducing the decreasing trends in measured groundwater. Our trends in runoff are consistent with the trends in runoff provided by Ghiggi et al.[79] in low elevation areas of the Ganges-Brahmaputra, over the Himalayas, our model indicates decreasing trends in runoff whereas the global runoff data indicates increasing trends such inconsistencies may arise from the differences in meteorological forcing. As shown in Supplementary Figure 7, the increasing trends in simulated ET were consistent with the trends in the MODIS[80] ET and the Global Land Evaporation Amsterdam Model (GLEAM[81]) ET. Finally, we also evaluate the probabilities of detection and false alarm of snow cover of our multivariate assimilation by relying on the snow cover data provided by MODIS[77]. As depicted in Supplementary Figure 8, the probability of detection is high (i.e., greater than 75%) over the Himalayas, however, the false alarm ratio reaches 50% in the upper regions of the Himalayas.

Data and Code Availability

The Nasa Land Information System (LIS) used in this study is an open-source software that can be found here: https://github.com/NASA-LIS/LISF

Datasets used in this study can be found in the following websites:

- HMA land reanalysis: https://nsidc.org/data/hma2_nlsmr/versions/1
- ERA5 forcing: https://www.ecmwf.int/en/forecasts/dataset/ecmwf-reanalysis-v5
- IMERG Precipitation: https://gpm.nasa.gov/taxonomy/term/1372
- CHIRPS Precipitation: https://www.chc.ucsb.edu/data
- SWE reconstruction by Kraaijenbrink et al., (2021): https://zenodo.org/record/4715786#.YqDY0S-B1pI
- MODIS LAI: https://lpdaac.usgs.gov/products/mcd15a2hv006/
- ESA CCI soil moisture: https://www.esa-soilmoisture-cci.org/data
- GRACE data: https://earth.gsfc.nasa.gov/geo/data/grace-mascons

Competing interests

The authors declare that they have no conflict of interest.

Author contribution

F.Z.M, A.G., and S.V.K. contributed with conceptualization, data analysis, and writing.

M.S., N.K.B., S.M., and R.A. contributed with the data acquisition.

S.V.K. was responsible for funding acquisition. All authors have read and agreed to the published version of the manuscript.

Acknowledgements

This research was supported by the grant from the National Aeronautics and Space Administration High Mountain Asia program (19-HMA19-0012). Computing was supported by the resources at the NASA Center for Climate Simulation.

References

1. Immerzeel, W. W., Beek, L. P. H. van & Bierkens, M. F. P. Climate Change Will Affect the Asian Water Towers. *Science* **328**, 1382–1385 (2010).
2. Pritchard, H. D. Asia's shrinking glaciers protect large populations from drought stress. *Nature* **569**, 649–654 (2019).
3. Qiu, J. China: The third pole. *Nature* **454**, 393–396 (2008).
4. Centre, U. W. H. The Sundarbans. *UNESCO World Heritage Centre* https://whc.unesco.org/en/list/798/.
5. Getirana, A. *et al.* Avert Bangladesh's looming water crisis through open science and better data. *Nature* **610**, 626–629 (2022).
6. Matsuo, K. & Heki, K. Time-variable ice loss in Asian high mountains from satellite gravimetry. *Earth and Planetary Science Letters* **290**, 30–36 (2010).
7. Smith, T. & Bookhagen, B. Changes in seasonal snow water equivalent distribution in High Mountain Asia (1987 to 2009). *Sci Adv* **4**, (2018).
8. Treichler, D., Kääb, A., Salzmann, N. & Xu, C.-Y. Recent glacier and lake changes in High Mountain Asia and their relation to precipitation changes. *The Cryosphere* **13**, 2977–3005 (2019).
9. Li, Y., Chen, Y., Wang, F., He, Y. & Li, Z. Evaluation and projection of snowfall changes in High Mountain Asia based on NASA's NEX-GDDP high-resolution daily downscaled dataset. *Environ. Res. Lett.* **15**, 104040 (2020).
10. Maina, F. Z. & Kumar, S. V. Diverging Trends in Rain-On-Snow Over High Mountain Asia. *Earth's Future* **11**, e2022EF003009 (2023).

11. Gleeson, T., Wada, Y., Bierkens, M. F. P. & van Beek, L. P. H. Water balance of global aquifers revealed by groundwater footprint. *Nature* **488**, 197–200 (2012).
12. Siebert, S. *et al.* Groundwater use for irrigation - a global inventory. *Hydrology and Earth System Sciences* **14**, 1863–1880 (2010).
13. Wada, Y., van Beek, L. P. H. & Bierkens, M. F. P. Nonsustainable groundwater sustaining irrigation: A global assessment. *Water Resources Research* **48**, (2012).
14. Mishra, V., Asoka, A., Vatta, K. & Lall, U. Groundwater Depletion and Associated CO2 Emissions in India. *Earth's Future* **6**, 1672–1681 (2018).
15. Dangar, S. & Mishra, V. Natural and anthropogenic drivers of the lost groundwater from the Ganga River basin. *Environ. Res. Lett.* **16**, 114009 (2021).
16. Goldin, T. India's drought below ground. *Nature Geosci* **9**, 98–98 (2016).
17. Rodell, M., Velicogna, I. & Famiglietti, J. S. Satellite-based estimates of groundwater depletion in India. *Nature* **460**, 999–1002 (2009).
18. Wada, Y. *et al.* Global depletion of groundwater resources. *Geophysical Research Letters* **37**, (2010).
19. Mukherjee, A., Bhanja, S. N. & Wada, Y. Groundwater depletion causing reduction of baseflow triggering Ganges river summer drying. *Sci Rep* **8**, 12049 (2018).
20. Chen, C. *et al.* China and India lead in greening of the world through land-use management. *Nature Sustainability* **2**, 122–129 (2019).
21. Maina, F. Z., Kumar, S. V., Albergel, C. & Mahanama, S. P. Warming, increase in precipitation, and irrigation enhance greening in High Mountain Asia. *Commun Earth Environ* **3**, 1–8 (2022).

22. Piao, S. *et al.* Characteristics, drivers and feedbacks of global greening. *Nature Reviews Earth & Environment* **1**, 14–27 (2020).

23. Zhu, Z. *et al.* Greening of the Earth and its drivers. *Nature Climate Change* **6**, 791–795 (2016).

24. Maina, F. Z., Kumar, S. V. & Gangodagamage, C. Irrigation and warming drive the decreases in surface albedo over High Mountain Asia. *Sci Rep* **12**, 16163 (2022).

25. Famiglietti, J. S. The global groundwater crisis. *Nature Climate Change* **4**, 945–948 (2014).

26. Niu, G.-Y. *et al.* The community Noah land surface model with multiparameterization options (Noah-MP): 1. Model description and evaluation with local-scale measurements. *Journal of Geophysical Research: Atmospheres* **116**, (2011).

27. Alam, S., Ali, Md. M., Rahaman, A. Z. & Islam, Z. Multi-model ensemble projection of mean and extreme streamflow of Brahmaputra River Basin under the impact of climate change. *Journal of Water and Climate Change* **12**, 2026–2044 (2021).

28. Anand, J., Gosain, A. K., Khosa, R. & Srinivasan, R. Regional scale hydrologic modeling for prediction of water balance, analysis of trends in streamflow and variations in streamflow: The case study of the Ganga River basin. *Journal of Hydrology: Regional Studies* **16**, 32–53 (2018).

29. Gain, A. K., Immerzeel, W. W., Sperna Weiland, F. C. & Bierkens, M. F. P. Impact of climate change on the stream flow of the lower Brahmaputra: trends in high and low flows based on discharge-weighted ensemble modelling. *Hydrology and Earth System Sciences* **15**, 1537–1545 (2011).

30. Masood, M., Yeh, P. J.-F., Hanasaki, N. & Takeuchi, K. Model study of the impacts of future climate change on the hydrology of Ganges–Brahmaputra–Meghna basin. *Hydrology and Earth System Sciences* **19**, 747–770 (2015).

31. Asoka, A. & Mishra, V. Anthropogenic and Climate Contributions on the Changes in Terrestrial Water Storage in India. *Journal of Geophysical Research: Atmospheres* **125**, e2020JD032470 (2020).

32. Wada, Y. & Bierkens, M. F. P. Sustainability of global water use: past reconstruction and future projections. *Environ. Res. Lett.* **9**, 104003 (2014).

33. Palazzi, E., Hardenberg, J. von & Provenzale, A. Precipitation in the Hindu-Kush Karakoram Himalaya: Observations and future scenarios. *Journal of Geophysical Research: Atmospheres* **118**, 85–100 (2013).

34. Yoon, Y. *et al.* Evaluating the Uncertainty of Terrestrial Water Budget Components Over High Mountain Asia. *Front. Earth Sci.* **7**, (2019).

35. You, Q., Min, J., Zhang, W., Pepin, N. & Kang, S. Comparison of multiple datasets with gridded precipitation observations over the Tibetan Plateau. *Clim Dyn* **45**, 791–806 (2015).

36. Maina, F. Z., Kumar, S. V., Dollan, I. J. & Maggioni, V. Development and evaluation of ensemble consensus precipitation estimates over High Mountain Asia. *Journal of Hydrometeorology* **1**, (2022).

37. Huffman, G. J., Bolvin, D. T. & Nelkin, E. J. Integrated Multi-satellitE Retrievals for GPM (IMERG) technical documentation. *NASA/GSFC Code* **612**, 47 (2015).

38. Funk, C. *et al.* The climate hazards infrared precipitation with stations—a new environmental record for monitoring extremes. *Scientific Data* **2**, 150066 (2015).

39. Hersbach, H. *et al.* The ERA5 global reanalysis. *Quarterly Journal of the Royal Meteorological Society* **146**, 1999–2049 (2020).

40. Clark, A. J. Generation of Ensemble Mean Precipitation Forecasts from Convection-Allowing Ensembles. *Weather and Forecasting* **32**, 1569–1583 (2017).

41. Kumar, S. V. *et al.* Land information system: An interoperable framework for high resolution land surface modeling. *Environmental Modelling & Software* **21**, 1402–1415 (2006).

42. Dickinson, R. E. Land Surface Processes and Climate—Surface Albedos and Energy Balance. in *Advances in Geophysics* (ed. Saltzman, B.) vol. 25 305–353 (Elsevier, 1983).

43. Niu, G.-Y. & Yang, Z.-L. Effects of vegetation canopy processes on snow surface energy and mass balances. *Journal of Geophysical Research: Atmospheres* **109**, (2004).

44. Dickinson, R. E., Shaikh, M., Bryant, R. & Graumlich, L. Interactive Canopies for a Climate Model. *Journal of Climate* **11**, 2823–2836 (1998).

45. Ball, J. T., Woodrow, I. E. & Berry, J. A. A Model Predicting Stomatal Conductance and its Contribution to the Control of Photosynthesis under Different Environmental Conditions. in *Progress in Photosynthesis Research: Volume 4 Proceedings of the VIIth International Congress on Photosynthesis Providence, Rhode Island, USA, August 10–15, 1986* (ed. Biggins, J.) 221–224 (Springer Netherlands, 1987). doi:10.1007/978-94-017-0519-6_48.

46. Richards, L. A. Capillary conduction of liquids through porous medium. *Journal of Applied Physics* **1**, 318–333 (1931).

47. Niu, G.-Y., Yang, Z.-L., Dickinson, R. E. & Gulden, L. E. A simple TOPMODEL-based runoff parameterization (SIMTOP) for use in global climate models. *Journal of Geophysical Research: Atmospheres* **110**, (2005).

48. Niu, G.-Y., Yang, Z.-L., Dickinson, R. E., Gulden, L. E. & Su, H. Development of a simple groundwater model for use in climate models and evaluation with Gravity Recovery and Climate Experiment data. *Journal of Geophysical Research: Atmospheres* **112**, (2007).

49. Xue, Y. *et al.* Assimilation of Satellite-Based Snow Cover and Freeze/Thaw Observations Over High Mountain Asia. *Front. Earth Sci.* **7**, (2019).

50. Xue, Y. *et al.* Evaluation of High Mountain Asia-Land Data Assimilation System (Version 1) From 2003 to 2016: 2. The Impact of Assimilating Satellite-Based Snow Cover and Freeze/Thaw Observations Into a Land Surface Model. *Journal of Geophysical Research: Atmospheres* **127**, e2021JD035992 (2022).

51. Yamazaki, D. *et al.* A high-accuracy map of global terrain elevations. *Geophysical Research Letters* **44**, 5844–5853 (2017).

52. Friedl, Mark & Sulla-Menashe, Damien. MCD12Q1 MODIS/Terra+Aqua Land Cover Type Yearly L3 Global 500m SIN Grid V006. (2019) doi:10.5067/MODIS/MCD12Q1.006.

53. ISRIC — World Soil Information. *ISRIC — World Soil Information* https://www.isric.org.

54. Getirana, A. C. V. *et al.* The Hydrological Modeling and Analysis Platform (HyMAP): Evaluation in the Amazon Basin. *Journal of Hydrometeorology* **13**, 1641–1665 (2012).

55. Getirana, A., Peters-Lidard, C., Rodell, M. & Bates, P. D. Trade-off between cost and accuracy in large-scale surface water dynamic modeling. *Water Resources Research* **53**, 4942–4955 (2017).

56. Yamazaki, D. *et al.* MERIT Hydro: A High-Resolution Global Hydrography Map Based on Latest Topography Dataset. *Water Resources Research* (2019) doi:10.1029/2019WR024873.

57. Reichle, R. H. Data assimilation methods in the Earth sciences. *Advances in Water Resources* **31**, 1411–1418 (2008).

58. Clark, M. P. *et al.* Hydrological data assimilation with the ensemble Kalman filter: Use of streamflow observations to update states in a distributed hydrological model. *Advances in Water Resources* **31**, 1309–1324 (2008).

59. Zhou, Y. *et al. Satellite-informed simulation of irrigation in South Asia: opportunities and uncertainties*. https://essopenarchive.org/doi/full/10.1002/essoar.10512174.1 (2022) doi:10.1002/essoar.10512174.1.

60. Dorigo, W. *et al.* ESA CCI Soil Moisture for improved Earth system understanding: State-of-the art and future directions. *Remote Sensing of Environment* **203**, 185–215 (2017).

61. Myneni, Ranga, Knyazikhin, Yuri & Park, Taejin. MOD15A2H MODIS/Terra Leaf Area Index/FPAR 8-Day L4 Global 500m SIN Grid V006. (2015) doi:10.5067/MODIS/MOD15A2H.006.

62. Kraaijenbrink, P. D. A., Stigter, E. E., Yao, T. & Immerzeel, W. W. Climate change decisive for Asia’s snow meltwater supply. *Nat. Clim. Chang.* **11**, 591–597 (2021).

63. Loomis, B. D., Felikson, D., Sabaka, T. J. & Medley, B. High-Spatial-Resolution Mass Rates From GRACE and GRACE-FO: Global and Ice Sheet Analyses. *Journal of Geophysical Research: Solid Earth* **126**, e2021JB023024 (2021).

64. Reichle, R. H., McLaughlin, D. B. & Entekhabi, D. Hydrologic Data Assimilation with the Ensemble Kalman Filter. *Monthly Weather Review* **130**, 103–114 (2002).

65. Zaitchik, B. F., Rodell, M. & Reichle, R. H. Assimilation of GRACE Terrestrial Water Storage Data into a Land Surface Model: Results for the Mississippi River Basin. *Journal of Hydrometeorology* **9**, 535–548 (2008).

66. Kumar, S. V. *et al.* Assimilation of Remotely Sensed Soil Moisture and Snow Depth Retrievals for Drought Estimation. *Journal of Hydrometeorology* **15**, 2446–2469 (2014).

67. Lahmers, T. M. *et al.* Assimilation of NASA’s Airborne Snow Observatory Snow Measurements for Improved Hydrological Modeling: A Case Study Enabled by the Coupled LIS/WRF-Hydro System. *Water Resources Research* **58**, e2021WR029867 (2022).

68. Liu, Y. *et al.* Assimilating satellite-based snow depth and snow cover products for improving snow predictions in Alaska. *Advances in Water Resources* **54**, 208–227 (2013).

69. Reichle, R. H., Kumar, S. V., Mahanama, S. P. P., Koster, R. D. & Liu, Q. Assimilation of Satellite-Derived Skin Temperature Observations into Land Surface Models. *Journal of Hydrometeorology* **11**, 1103–1122 (2010).

70. Slater, A. G. & Clark, M. P. Snow Data Assimilation via an Ensemble Kalman Filter. *Journal of Hydrometeorology* **7**, 478–493 (2006).

71. Ambika, A. K., Wardlow, B. & Mishra, V. Remotely sensed high resolution irrigated area mapping in India for 2000 to 2015. *Scientific Data* **3**, 160118 (2016).

72. Nie, W. *et al.* Groundwater Withdrawals Under Drought: Reconciling GRACE and Land Surface Models in the United States High Plains Aquifer. *Water Resources Research* **54**, 5282–5299 (2018).

73. Kumar, S. V. *et al.* A comparison of methods for a priori bias correction in soil moisture data assimilation. *Water Resources Research* **48**, (2012).

74. Kumar, S. V. *et al.* NCA-LDAS Land Analysis: Development and Performance of a Multisensor, Multivariate Land Data Assimilation System for the National Climate Assessment. *Journal of Hydrometeorology* **20**, 1571–1593 (2019).

75. Liu, X., Chen, F., Barlage, M., Zhou, G. & Niyogi, D. Noah-MP-Crop: Introducing dynamic crop growth in the Noah-MP land surface model. *Journal of Geophysical Research: Atmospheres* **121**, 13,953-13,972 (2016).

76. Hock, R. Temperature index melt modelling in mountain areas. *Journal of Hydrology* **282**, 104–115 (2003).

77. Hall, Dorothy, George, K., Riggs, A. & Salomonson, Vincent V. MODIS/Terra Snow Cover 5-Min L2 Swath 500m, Version 5. (2006) doi:10.5067/ACYTYZB9BEOS.

78. Kumar, S. V. *et al.* Assimilation of Gridded GRACE Terrestrial Water Storage Estimates in the North American Land Data Assimilation System. *J. Hydrometeor.* **17**, 1951–1972 (2016).

79. Ghiggi, G., Humphrey, V., Seneviratne, S. I. & Gudmundsson, L. G-RUN ENSEMBLE: A Multi-Forcing Observation-Based Global Runoff Reanalysis. *Water Resources Research* **57**, e2020WR028787 (2021).

80. Running, Steve, Mu, Qiaozhen & Zhao, Maosheng. MOD16A2 MODIS/Terra Net Evapotranspiration 8-Day L4 Global 500m SIN Grid V006. (2017) doi:10.5067/MODIS/MOD16A2.006.

81. Martens, B. *et al.* GLEAM v3: satellite-based land evaporation and root-zone soil moisture. *Geoscientific Model Development* **10**, 1903–1925 (2017).

82. Salmon, J. M., Friedl, M. A., Frolking, S., Wisser, D. & Douglas, E. M. Global rain-fed, irrigated, and paddy croplands: A new high resolution map derived from remote sensing, crop inventories and climate data. *International Journal of Applied Earth Observation and Geoinformation* **38**, 321–334 (2015).

Figure Caption

Figure 1: The Ganges-Brahmaputra basin: irrigated areas[82], rivers in blue, basin in gray and political in black boundaries.

Figure 2: Annual trends in (a) streamflow, (b) precipitation, (c) terrestrial water storage (TWS), (d) surface runoff, (e) baseflow, and (f) snowmelt obtained with the reanalysis (i.e., the simulation with the effects of irrigation). (g) differences between the simulations with and without the effects of irrigation in the annual trends in streamflow. Trends were computed using the Mann-Kendall test with a confidence level of 95%, non-significant trends were set to 0. Despite the increases in precipitation, the streamflow has decreasing trends due to the decreases in TWS. The positive differences show that the negative trends of the streamflow are higher in the simulation with the effects of irrigation than in the one without.

Figure 3: Comparisons between the trends in streamflow obtained with the land reanalysis and the simulation only accounting for the changes in climate and without irrigation. Annual mean in black, minimum (i.e., baseflow) in red, maximum (i.e., peak flow) in blue simulated streamflow at two locations in the Ganges and the Brahmaputra rivers. The dots represent the values (mean, max, and min) obtained with the simulation only accounting for the changes in climate and without irrigation and the dotted lines represent their corresponding slopes (the values of these slopes are also indicated in the figure). The thick lines represent the values (mean, max, and min) obtained with the land reanalysis and the dashed lines represent their corresponding slopes (the values of these slopes are also indicated in the figure). The reanalysis has decreasing trends whereas the simulation without the effects of irrigation generally shows increasing trends.

Figure 4: Seasonal trends in (a) precipitation and (b) streamflow obtained with the reanalysis (i.e., the simulation with the effects of irrigation). Trends were computed using the Mann-Kendall test

with a confidence level of 95%, non-significant trends were set to 0. Despite the increases in precipitation (notably in MAM and JJA), the streamflow keeps decreasing for all seasons.

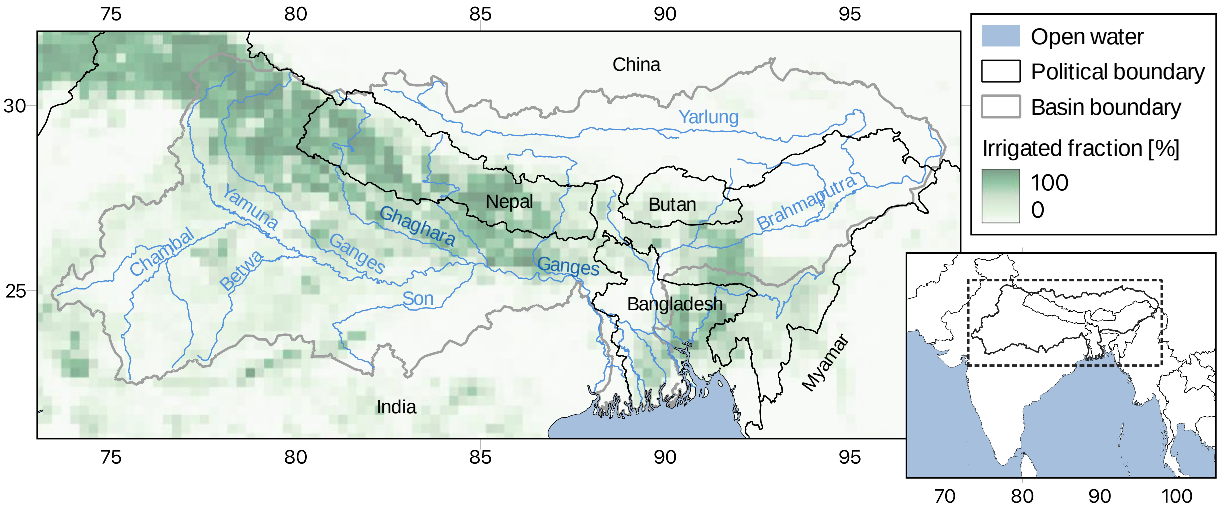

Figure 1: The Ganges-Brahmaputra basin: irrigated areas[82], rivers in blue, basin in gray and political in black boundaries.

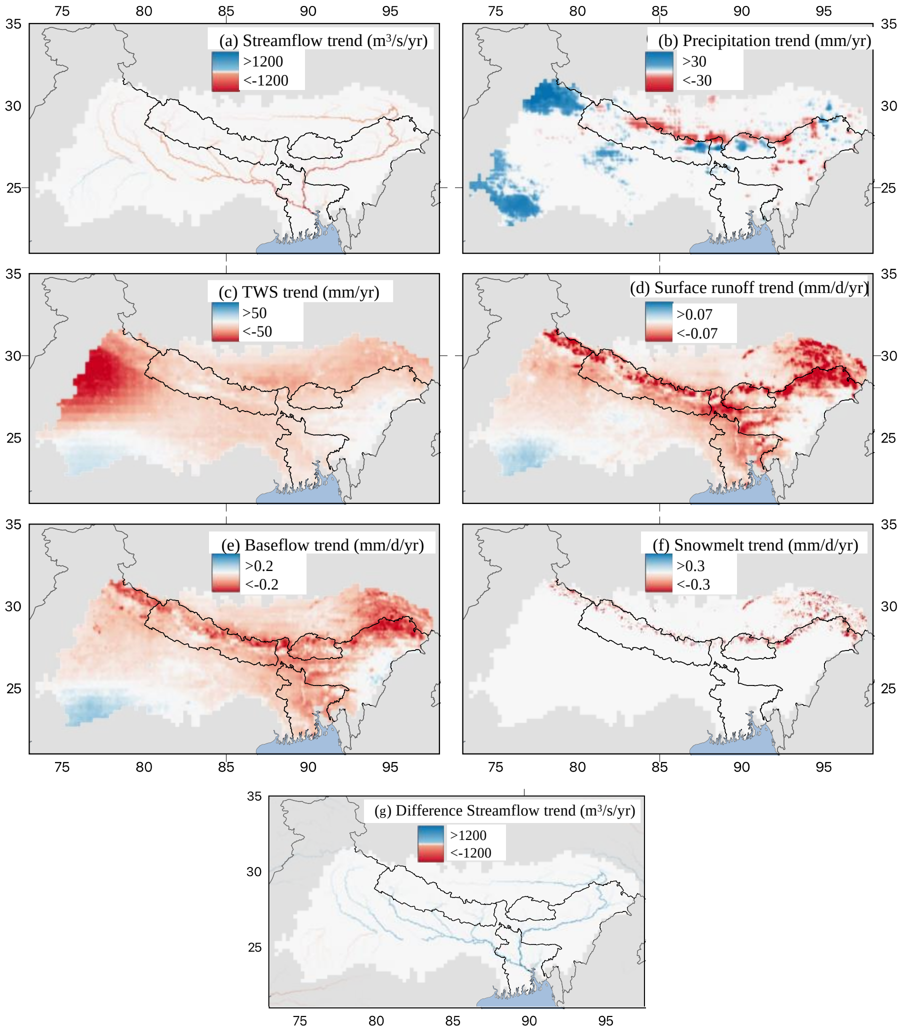

Figure 2: Annual trends in (a) streamflow, (b) precipitation, (c) terrestrial water storage (TWS), (d) surface runoff, (e) baseflow, and (f) snowmelt obtained with the reanalysis (i.e., the simulation with the effects of irrigation). (g) differences between the simulations with and without the effects of irrigation in the annual trends in streamflow. Trends were computed using the Mann-Kendall test with a confidence level of 95%, non-significant trends were set to 0. Despite the increases in precipitation, the streamflow has decreasing trends due to the decreases in TWS. The positive differences show that the negative trends of the streamflow are higher in the simulation with the effects of irrigation than in the one without.

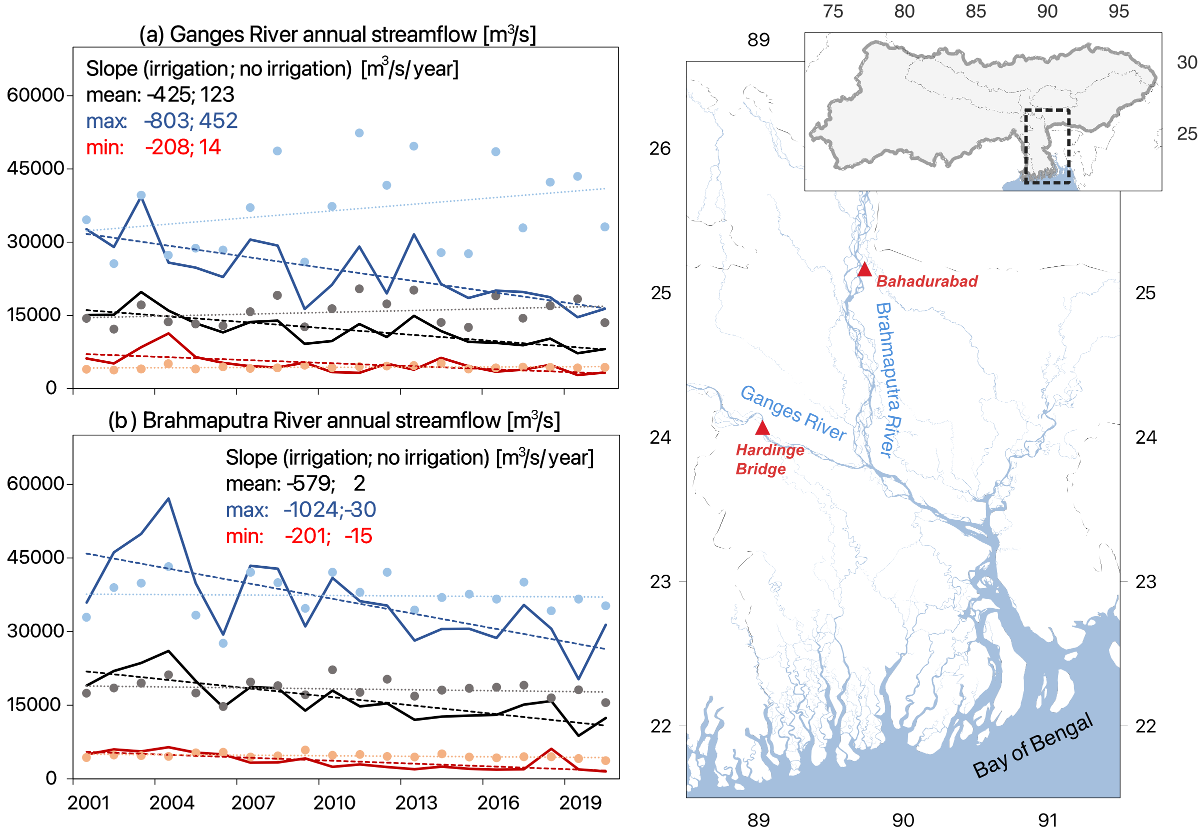

Figure 3: Comparisons between the trends in streamflow obtained with the land reanalysis and the simulation only accounting for the changes in climate and without irrigation. Annual mean in black, minimum (i.e., baseflow) in red, maximum (i.e., peak flow) in blue simulated streamflow at two locations in the Ganges and the Brahmaputra rivers. The dots represent the values (mean, max, and min) obtained with the simulation only accounting for the changes in climate and without irrigation and the dotted lines represent their corresponding slopes (the values of these slopes are also indicated in the figure). The thick lines represent the values (mean, max, and min) obtained with the land reanalysis and the dashed lines represent their corresponding slopes (the values of these slopes are also indicated in the figure). The reanalysis has decreasing trends whereas the simulation without the effects of irrigation generally shows increasing trends.

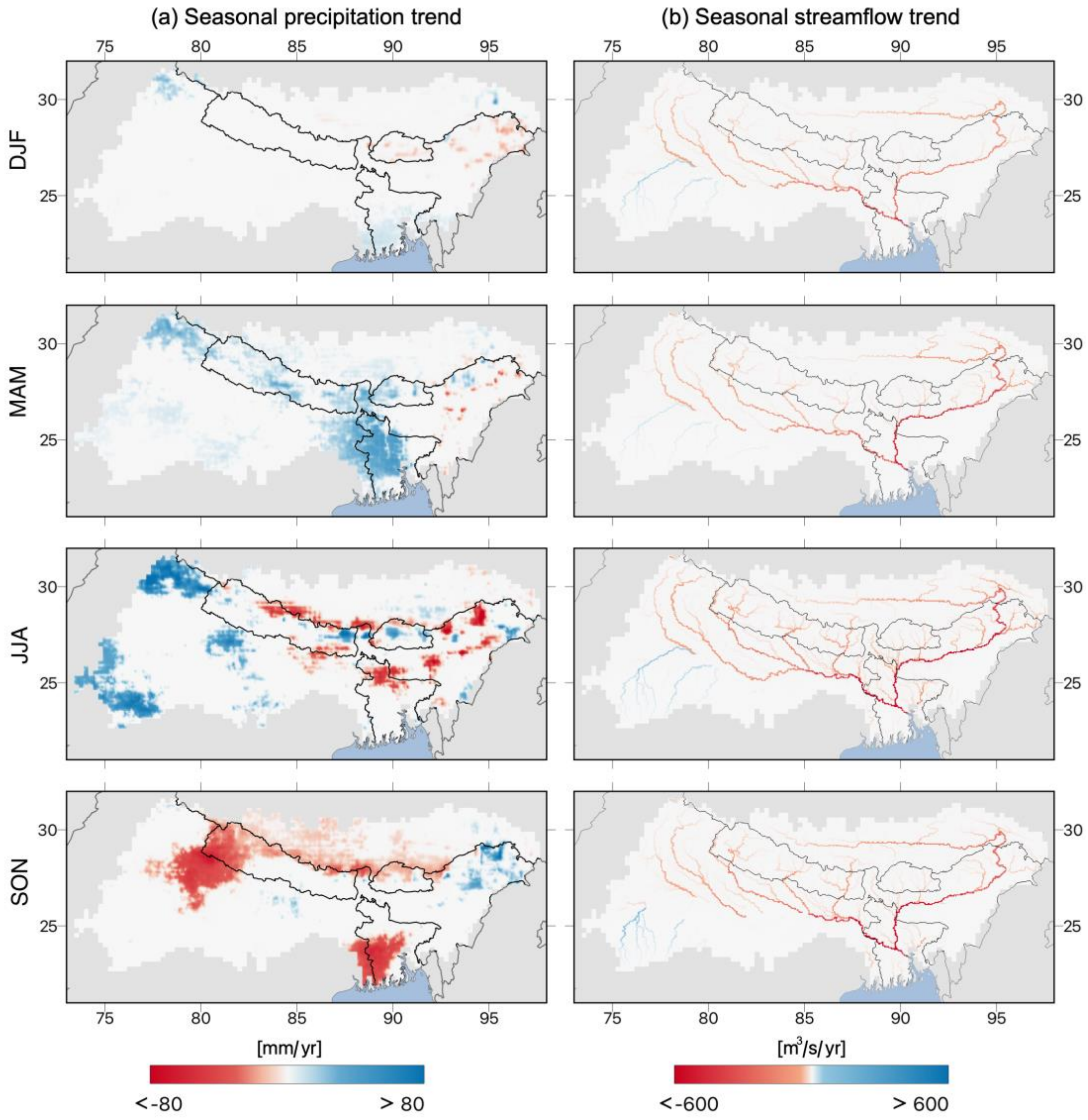

Figure 4: Seasonal trends in (a) precipitation and (b) streamflow obtained with the reanalysis (i.e., the simulation with the effects of irrigation). Trends were computed using the Mann-Kendall test with a confidence level of 95%, non-significant trends were set to 0. Despite the increases in precipitation (notably in MAM and JJA), the streamflow keeps decreasing for all seasons.

Supplementary Information

Variables	Type	Standard Deviation	Temporal Correlation	Perturbation cross-correlations
Forcing				
Precipitation	M	0.2	24h	1.0 -0.5 -0.8
Shortwave Radiation	M	30	24h	-0.5 1.0 0.5
Longwave Radiation	A	0.50	24h	-0.8 0.5 1.0
Assimilation of Soil Moisture				
ESA CCI Soil Moisture	A	0.02	12h	
Modeled Soil Moisture Layer 1	A	0.1	3h	1.0 0.6 0.4 0.2
Modeled Soil Moisture Layer 2	A	0.1	3h	0.6 1.0 0.6 0.4
Modeled Soil Moisture Layer 3	A	0.1	3h	0.4 0.6 1.0 0.6
Modeled Soil Moisture Layer 4	A	0.1	3h	0.2 0.4 0.6 1.0
Assimilation of LAI				
MODIS LAI	A	0.01	1 h	
Modeled LAI	A	0.01	1h	
Assimilation of SWE				
SWE Reconstruction	M	0.05	3h	
Modeled Snow Depth	M	0.01	3h	1.0 0.9
Modeled SWE	M	0.01	3h	0.9 1.0
Assimilation of GRACE				
GRACE TWS	A	5.0	24h	
Modeled Soil Moisture Layer 1	A	0.005	3h	1.0 0.6 0.4 0.2 0.0 0.0
Modeled Soil Moisture Layer 2	A	0.005	3h	0.6 1.0 0.6 0.4 0.0 0.0
Modeled Soil Moisture Layer 3	A	0.005	3h	0.4 0.6 1.0 0.6. 0.0 0.0
Modeled Soil Moisture Layer 4	A	0.005	3h	0.2 0.4 0.6 1.0 0.0 0.0
Modeled Groundwater Storage	A	0.1	3h	0.0 0.0 0.0 0.0 0.0 1.0 0.0
Modeled SWE	M	0.001	30min	0.0 0.0 0.0 0.0 0.0 0.0 1.0

Supplementary Table 1: Applied perturbations for the multivariate data assimilation

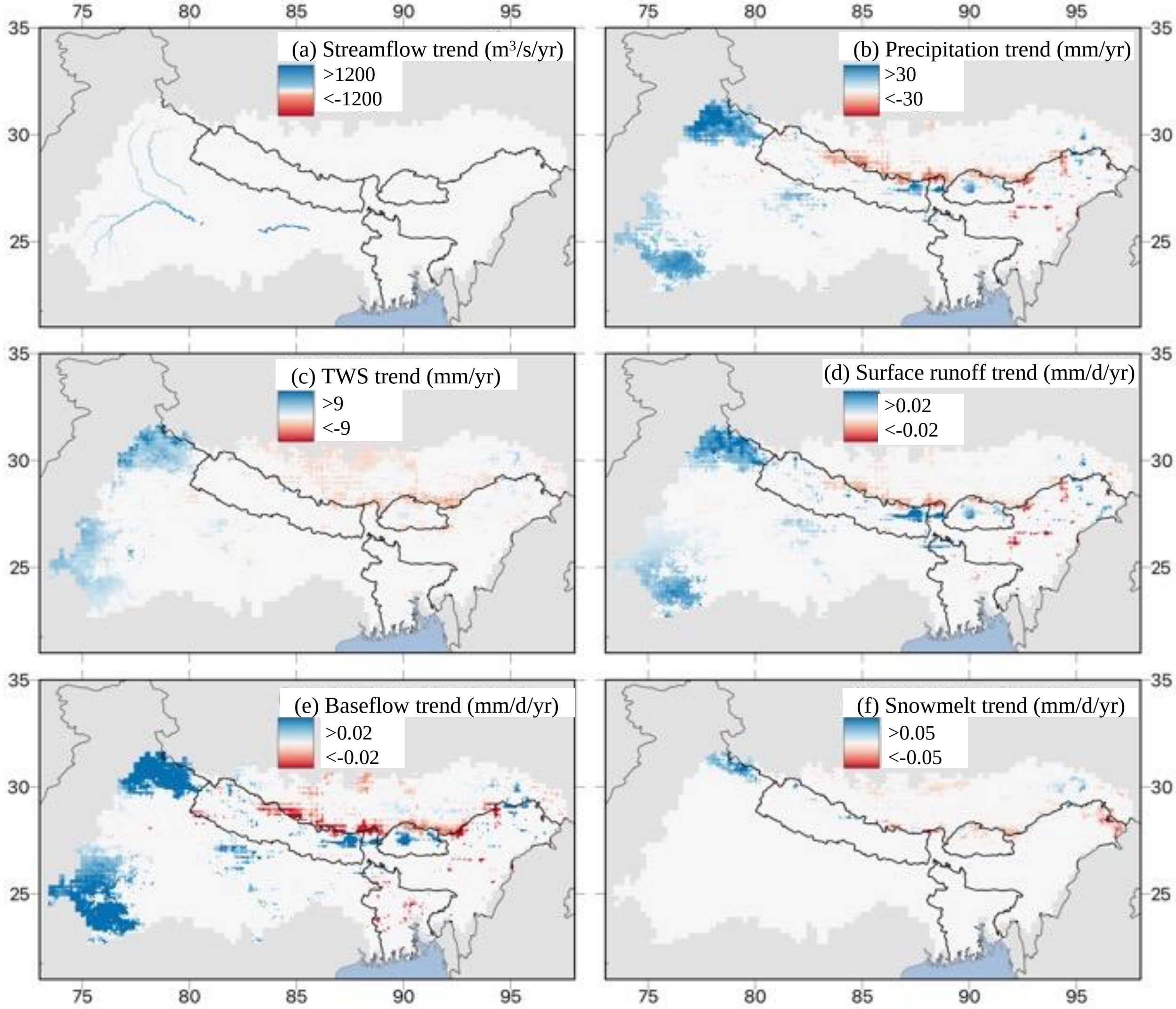

Supplementary Figure 1: Annual trends in (a) streamflow, (b) precipitation, (c) Terrestrial Water Storages, (d) surface runoff, (e) baseflow, and (f) snowmelt obtained with the simulation without the effects of irrigation. Trends were computed using the Mann-Kendall test with a confidence level of 95%, non-significant trends were set to 0. On contrary the land reanalysis, the simulation without the effects of irrigation has positive trends in streamflow due to an increase in precipitation.

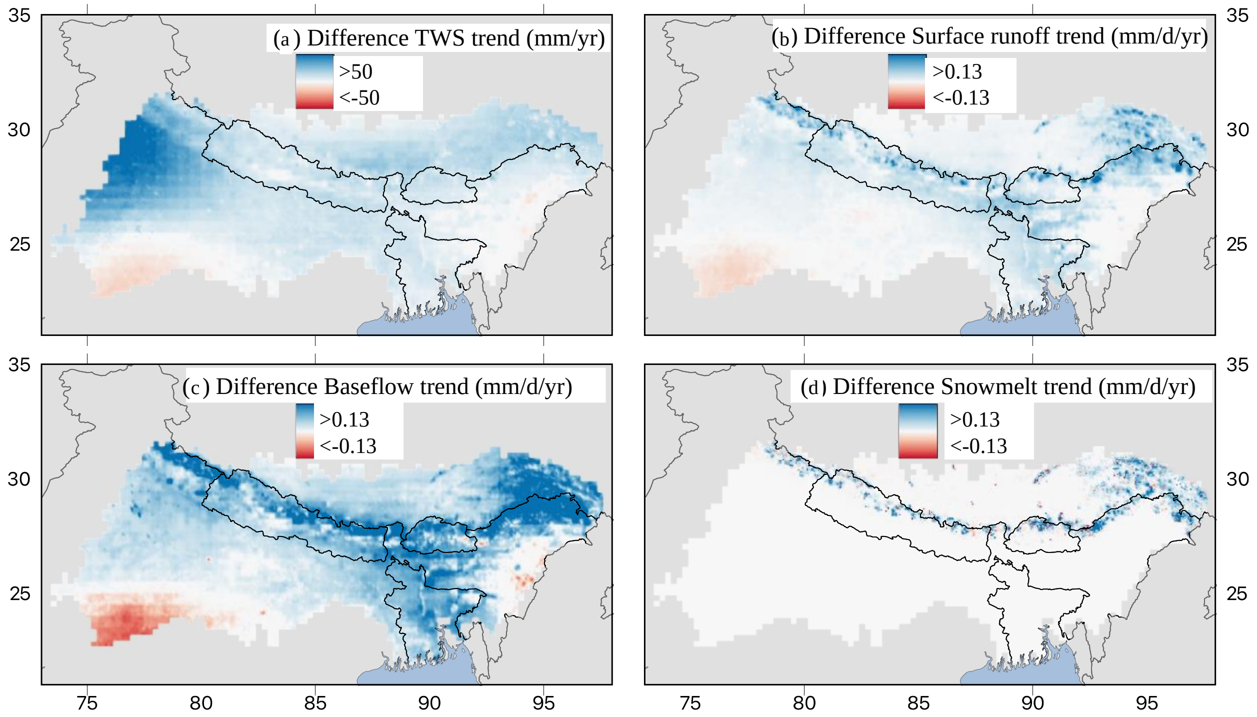

Supplementary Figure 2: Differences between the simulations with and without the effects of irrigation in the annual trends in (a) Terrestrial Water Storages, (b) surface runoff, (c) baseflow, and (d) snowmelt. Trends were computed using the Mann-Kendall test with a confidence level of 95%, non-significant trends were set to 0. The positive differences show that the negative trends of these variables are higher in the with the simulation effects of irrigation than in the one without.

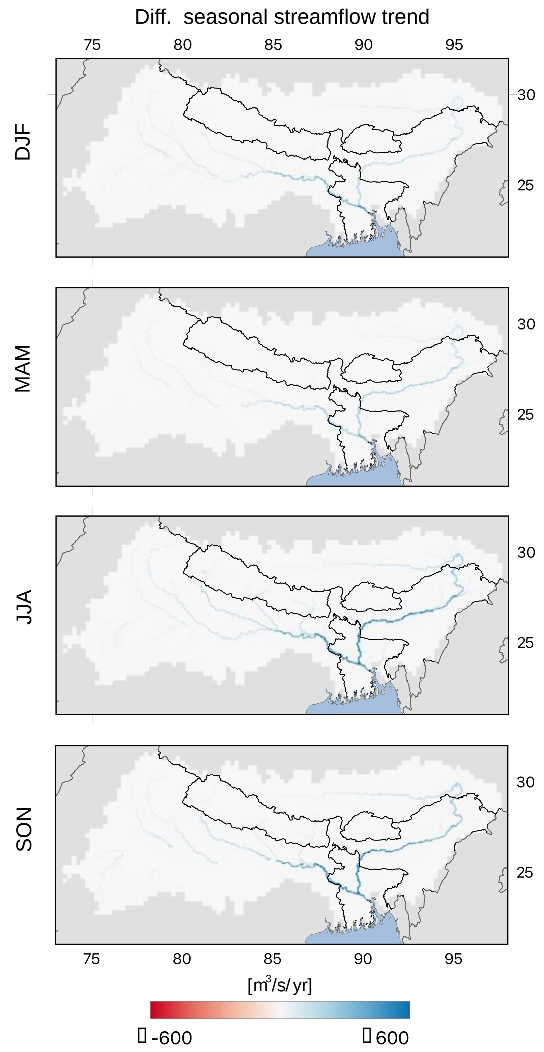

Supplementary Figure 3: Differences between the simulations with and without the effects of irrigation in seasonal trends in streamflow. Trends were computed using the Mann-Kendall test with a confidence level of 95%, non-significant trends were set to 0. The positive differences show that the negative trends of these variables are higher in the simulation with the effects of irrigation than in the one without.

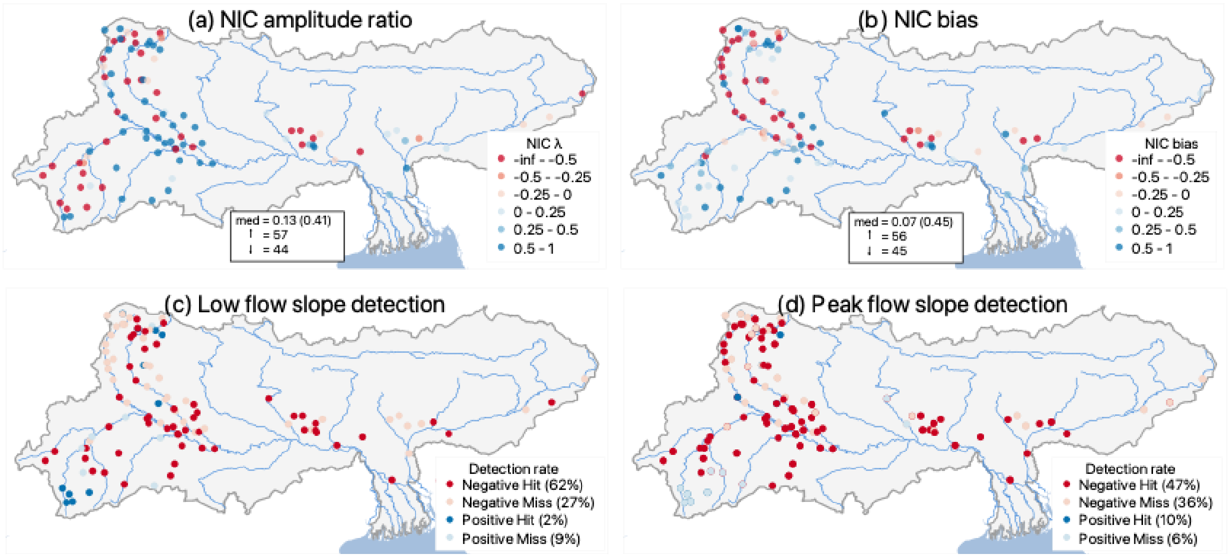

Supplementary Figure 4: Streamflow evaluation at 100 gauges within the Ganges-Brahmaputra basin. Upper panels show the normalized information contribution (NIC) metric applied to (a) the amplitude ratio and (b) bias. Boxes at the bottom of panels (a) and (b) show median NIC values for all gauges (and mean for gauges located near the outlet) and number of wells with improved (↑) and degraded (↓)metrics. Lower panels show slope detection rates for (c) low and (d) peak flows. "Negative Hit" are locations where both observed and simulated streamflow have negative slope, in "Negative Miss" observations have negative slope and simulations positive, in "Positive Hit" both observed and simulated streamflow have negative slope, and in "Positive Miss" observations have positive slope and simulations negative. Overall, the reanalysis captures the dynamics of the basin.

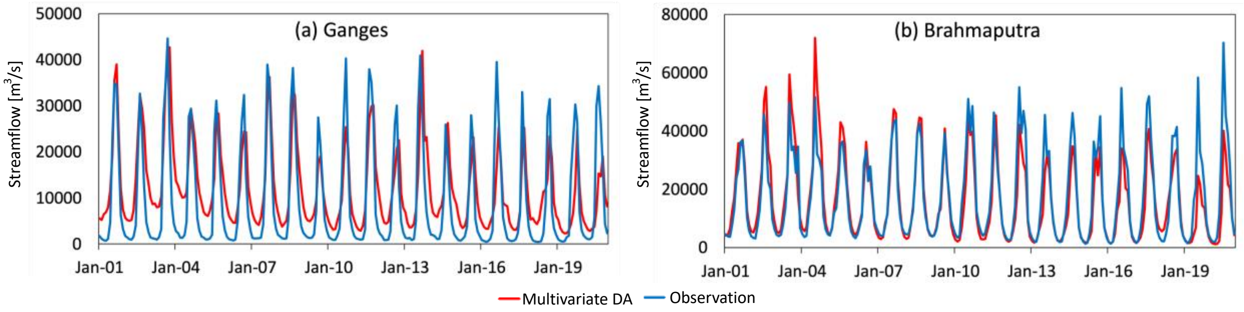

Supplementary Figure 5: Monthly streamflow time series over the 2000-2020 period at gauges located in the (a) Ganges and (b) Brahmaputra Rivers, near the outlet (see Figure 3 for locations). The blue line indicates the observations and the red line the results of the land reanalysis. While the reanalysis captures the observed trends in streamflow, it underestimates peak flow in both the Ganges and the Brahmaputra basins, and overestimates baseflow in the Brahmaputra basin.

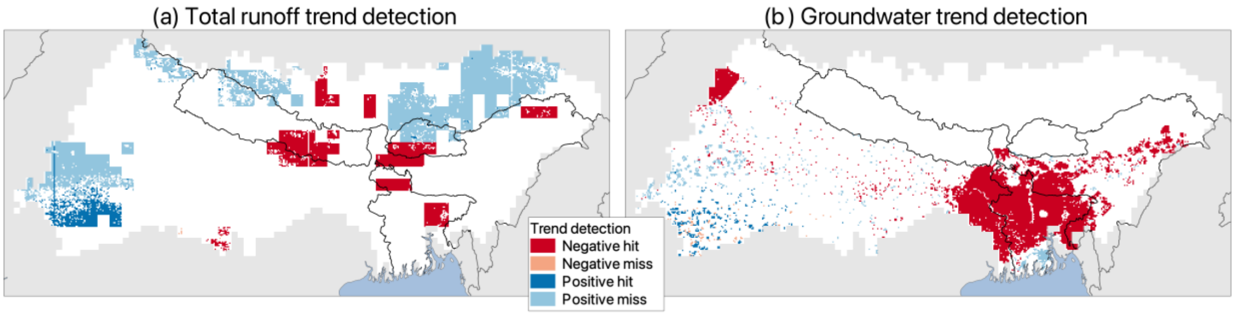

Supplementary Figure 6: Trends detection for (a) runoff (based on the global runoff data provided by[79]) and (b) groundwater storage. "Negative Hit" are locations where both observed/remotely sensed and simulated values have negative trends, in "Negative Miss" observations have negative trends and simulations positive, in "Positive Hit" both observed/remotely sensed and simulated values have negative trends, and in "Positive Miss" observations have positive trends and simulations negative. The reanalysis captures the measured trends in groundwater levels, however, the performance on the trends in global runoff is not as good as for the groundwater levels likely because the global runoff dataset is derived from a model entitled with uncertainties.

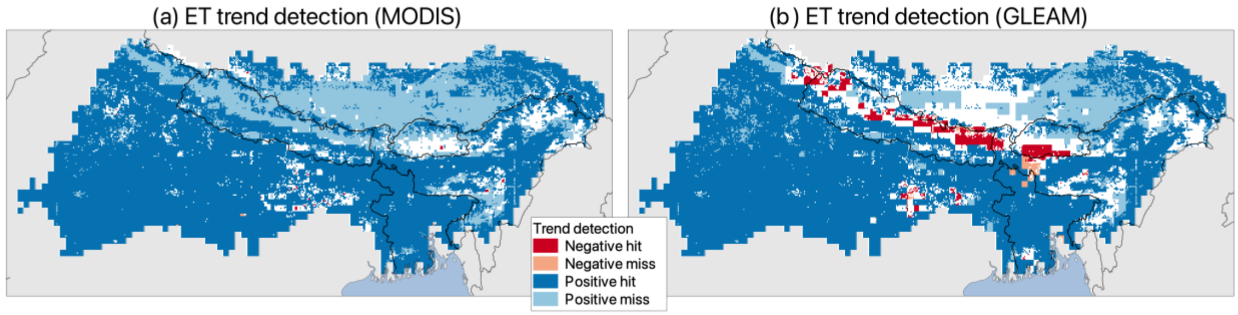

Supplementary Figure 7: Trends detection for ET compared to (a) the Moderate Resolution Imaging Spectroradiometer (MODIS[80]) and (b) the Global Land Evaporation Amsterdam Model (GLEAM[81]). "Negative Hit" are locations where both remotely sensed and simulated values have negative trends, in "Negative Miss" observations have negative trends and simulations positive, in "Positive Hit" both remotely sensed and simulated values have negative trends, and in "Positive Miss" observations have positive trends and simulations negative. The reanalysis captures the trends in ET provided by MODIS and GLEAM.

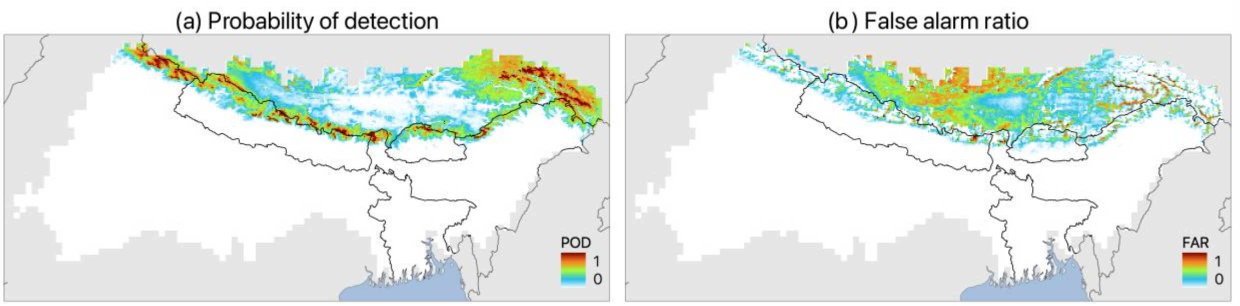

Supplementary Figure 8: Spatial distributions of the probabilities of (a) detection (POD annual average), (b) false alarm (FAR annual average) of the assimilation results compared to the snow cover provided by the Moderate Resolution Imaging Spectroradiometer (MODIS)[77]. The probability of detection of the reanalysis is close to 1 at many points.